

Space environment of an asteroid preserved on micrograins returned by the Hayabusa spacecraft

Eizo Nakamura^{a,1}, Akio Makishima^a, Takuya Moriguti^a, Katsura Kobayashi^a, Ryoji Tanaka^a, Tak Kunihiro^a, Tatsuki Tsujimori^a, Chie Sakaguchi^a, Hiroshi Kitagawa^a, Tsutomu Ota^a, Yusuke Yachi^a, Toru Yada^b, Masanao Abe^b, Akio Fujimura^b, Munetaka Ueno^b, Toshifumi Mukai^b, Makoto Yoshikawa^b, and Jun'ichi Kawaguchi^b

^aThe Pheasant Memorial Laboratory for Geochemistry and Cosmochemistry, Institute for Study of the Earth's Interior, Okayama University, Misasa, Tottori 682-0193, Japan; and ^bJapan Aerospace Exploration Agency, Yoshinodai 3-1-1, Chuo, Sagami-hara, Kanagawa 252-5210, Japan

Edited by* Ikuro Kushiro, University of Tokyo, Tokyo, Japan, and approved January 28, 2012 (received for review October 4, 2011)

Records of micrometeorite collisions at down to submicron scales were discovered on dust grains recovered from near-Earth asteroid 25143 (Itokawa). Because the grains were sampled from very near the surface of the asteroid, by the Hayabusa spacecraft, their surfaces reflect the low-gravity space environment influencing the physical nature of the asteroid exterior. The space environment was examined by description of grain surfaces and asteroidal scenes were reconstructed. Chemical and O isotope compositions of five lithic grains, with diameters near 50 μm , indicate that the uppermost layer of the rubble-pile-textured Itokawa is largely composed of equilibrated LL-ordinary-chondrite-like material with superimposed effects of collisions. The surfaces of the grains are dominated by fractures, and the fracture planes contain not only sub- μm -sized craters but also a large number of sub- μm - to several- μm -sized adhered particles, some of the latter composed of glass. The size distribution and chemical compositions of the adhered particles, together with the occurrences of the sub- μm -sized craters, suggest formation by hypervelocity collisions of micrometeorites at down to nm scales, a process expected in the physically hostile environment at an asteroid's surface. We describe impact-related phenomena, ranging in scale from 10^{-9} to 10^4 meters, demonstrating the central role played by impact processes in the long-term evolution of planetary bodies. Impact appears to be an important process shaping the exteriors of not only large planetary bodies, such as the moon, but also low-gravity bodies such as asteroids.

impacts | sample-return mission | interplanetary dust | space weathering | comprehensive analysis

Solar bodies have evolved from dust to planets with interactions between dust and debris, and asteroids are considered intermediate products of this evolution. Asteroids were not melted and retain their primitive morphology and geochemistry, thus allowing us to investigate interactions between solids and the solar nebula. Meteorites are regarded as fragments of asteroids that fall to Earth's surface. However, information regarding the outer surface of asteroids is presumably destroyed during atmospheric entry, preventing examination of solar space-exposed exteriors of planetary bodies other than that of the moon sampled by the Apollo missions. Nearly all the materials now residing in the planets were processed through high-velocity impacts; however, previous investigation of collisional processes on low-gravity solar bodies has been limited to remote observations by satellites, with no direct sampling of such bodies.

The Japan Aerospace Exploration Agency (JAXA) conducted the Hayabusa mission with the goal of better understanding solar system evolution through direct sampling of an asteroid and return of the samples to Earth for detailed analytical work. A target was set to the near-Earth asteroid 25143 Itokawa, an example of a spectral type-S asteroid common in the inner part of the asteroid belt. On-site observations by the spacecraft showed that Itokawa is $550 \times 298 \times 224$ m in size and has rubble-pile structure with a density of 1.9 g/cm^3 and an escape velocity of 0.2 m/s (1). An onboard multiband camera (AMICA) imaged the solid exterior

of the asteroid and revealed a diversity of surface morphologies (2, 3). Based on topography and spectroscopic observations, a sampling location on a smooth terrain called Muses Sea was selected.

The original plan of the mission was to collect rocks from Itokawa's surface by an impact sampling method. However, at the time of the touchdown, no projectile was fired (4), resulting in only minimal sample recovery. Collection of material from very near the surface resulted from gentle flicking by the tip of the sampler horn. The sample capsule was returned to Earth on June 13, 2010, and opened at a JAXA curation facility. As a part of the mission, initial analyses of returned grains were carried out by several teams of researchers. One team reported on the general properties of the grains and concluded that the building blocks of the rubble pile were identical to those of equilibrated LL-ordinary chondrites with mild overprinting by "space weathering" (5–8). This conclusion is consistent with the spectroscopic observations made from Earth and by the Hayabusa spacecraft (9, 10); however, some key questions remain. What record of the environment at the asteroid exterior exists on the surface of grains deposited there and, more broadly, what were the most important processes shaping the postaccretion appearance of this asteroid? Nanometer-scale investigation of the surfaces of these micrograins can help us characterize the space environment of this and other asteroids, an important step toward more general understanding of impact phenomena in the inner solar system.

In this paper, we summarize the results of our comprehensive initial analysis of the sizes, morphology, mineralogy, and geochemistry of five lithic grains from Itokawa. We in particular focus on grain surfaces and report discoveries of (i) craters with diameters of 100–200 nm that provide direct evidence of sub- μm -scale bombardment at the asteroid surface, and (ii) objects adhered to the surfaces of these grains and representing high-velocity impacts. We suggest that the space environment alters asteroid surfaces by a combination of disaggregation, cratering, melting, adhesion, agglutination, and implantation/sputtering, all consequences of constant bombardment by nm- to μm -scale particles. Our observations regarding the sub- μm -scale physical

Author contributions: E.N. undertook the initial analysis; A.M. and T. Moriguti prepared reference materials; K.K. coordinated the flow of the analytical work through the laboratories and performed the FIB slabbing of the grains; R.T. analyzed oxygen isotopes for the reference materials; T.K. carried out in situ oxygen-isotope analyses; T.T. carried out petrographic and mineralogical investigations; C.S. evaluated adhered objects; H.K. assisted in the electron and ion probe work; T.O. determined elemental compositions; Y.Y. documented the sample status; T.Y., M.A., A.F., M.U., T. Mukai, M.Y., and J.K. worked on sample preparation; and E.N., A.M., T. Moriguti, K.K., R.T., T.K., and T.T. wrote the paper.

The authors declare no conflict of interest.

*This Direct Submission article had a prearranged editor.

Freely available online through the PNAS open access option.

¹To whom correspondence should be addressed. E-mail: eizonak@misasa.okayama-u.ac.jp.

See Author Summary on page 4031 (volume 109, number 11).

This article contains supporting information online at www.pnas.org/lookup/suppl/doi:10.1073/pnas.1116236109/-DCSupplemental.

and chemical changes on these grain surfaces help elucidate the process of space weathering that, at larger scales at an asteroid surface, produces a reddening and a reduction in band depth in spectroscopic observations.

Results

Mineralogical Properties of the Five Grains. The grains we investigated were 40–110 μm -sized, mono- or poly-phase fragments. Grains A–E surveyed in this study have JAXA-ID RA-QD02-0121, 0093, 0095, 0118, and 0116, respectively. All grains exhibit angular outlines and high surface relief. Grain A ($40 \times 30 \mu\text{m}$) consists of olivine and low-Ca pyroxene (Fig. 1*A*), with the olivine showing sets of sharply defined lamellae with widths at the sub- μm -scale (Fig. 1*B*). These lamellae could reflect high strain rates and high shear stresses associated with shock compression and have previously been referred to as shock lamellae (11). An object with a ropey fabric, observed on and along a crack crosscutting the lamellae, appears to have originated from melt (Fig. 1*C*). Grain B ($110 \times 90 \mu\text{m}$) is a fragment of a single olivine (Fig. 2*A*) with inclusions of oriented, very thin (10–20 μm), sub-parallel plates with the composition of plagioclase. This intergrowth resembles the “barred olivine” observed in chondrules (12) (Fig. 2*B*). A 1 μm -sized diopside is also included in this single olivine grain, and sub- μm -sized chromites are included in both the olivine and the plagioclase. Grain C ($70 \times 50 \mu\text{m}$) consists of diopside and plagioclase (Fig. 3*A*), with minor K-feldspar (Fig. 3*B*). A trail of microbowls crosscuts both the diopside and the plagioclase (Fig. 3*C*). These microbowls are filled with troilite, to varying degrees, perhaps reflecting some evaporation of troilite during thermal metamorphism. The plagioclase exhibits unusually low birefringence (Fig. 3*B*) suggesting that its structure is intermediate between crystalline and glassy. When observed in meteorites, such plagioclase is referred to as being diaplectic and indicative of shock metamorphism at certain impact pressures (13). The plagioclase in Grain C shows a sharp contact with diopside, likely reflecting formation by devitrification of chondrule

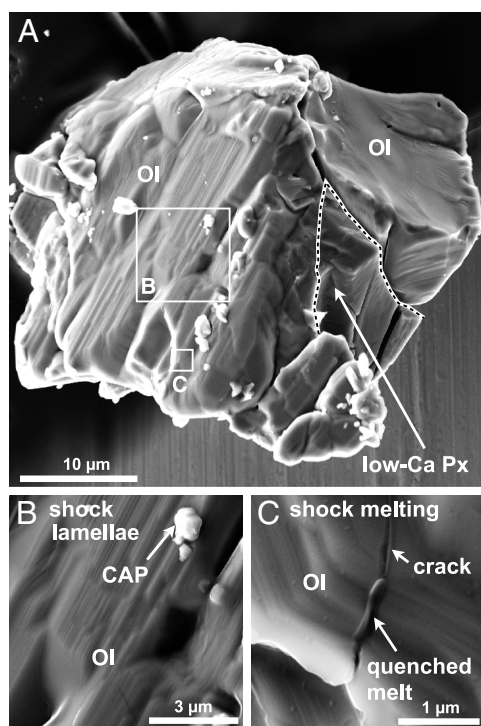


Fig. 1. Surface images obtained by SEM of Grain A with shock-induced textures. (A) The entire Grain A, indicating the locations for the higher-magnification images. (B) Shock lamellae developed on olivine (Ol). (C) Quenched melt on and along a crack crosscutting the shock lamellae.

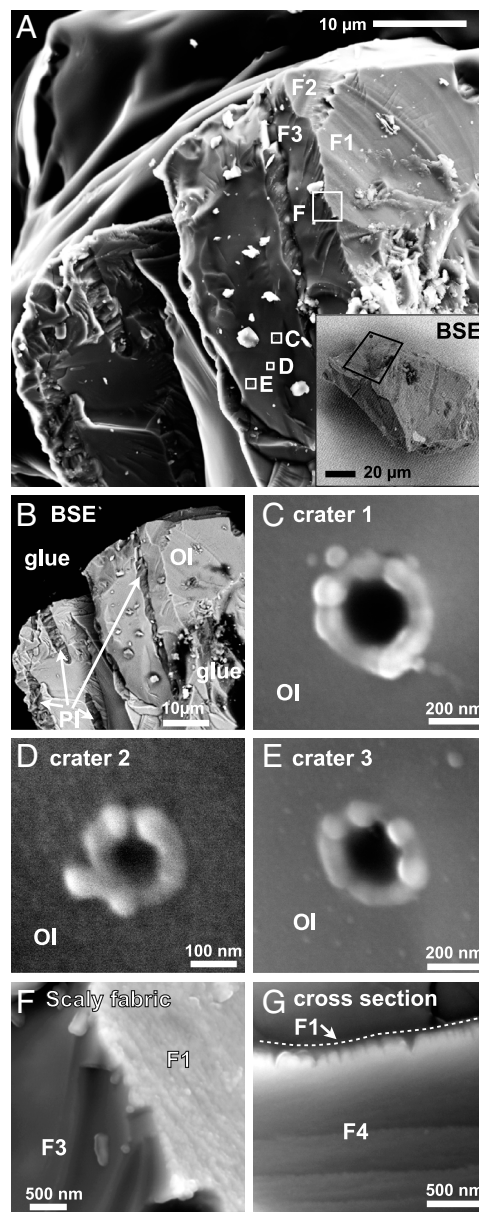


Fig. 2. Surface images (SEM unless otherwise specified) of Grain B with sub- μm -sized craters. (A) A part of Grain B, with the location on the complete grain indicated in the inserted BSE (back-scattered electron) image located in the SE part of the photograph. F1, F2, and F3 represent fracture planes, numbered in order of the relative timing of their formation (with F1 the earliest-form plane). (B) A BSE image of the region of (A), showing a barred-olivine texture. (C, D, E) Sub- μm -sized craters on Ol substrate. A pit rim with chains of seven or eight spheres. (F) An intersection of F1 and F3 and a scaly fabric on F1. (G) A cross section of the scaly fabric showing the sawtooth morphology on F1.

glass during the thermal metamorphism (14). Grain D is a fragment ($50 \times 40 \mu\text{m}$) of low-Ca pyroxene for which no inclusions or shock-related textures were observed. For Grain E ($50 \times 40 \mu\text{m}$), which also consists of low-Ca pyroxene, only surface observations were undertaken (Fig. 4*A*).

Grains were cut into three pieces, by focused-ion beam methods (FIB), for the electron and ion microprobe analyses (Fig. 3*A*). The middle slabs with two very flat, planar surfaces were used for these analyses and the other pieces were preserved for future work. In situ O isotope analyses were carried out by secondary-ion mass spectrometry (SIMS) on Grains A–D. The analytical

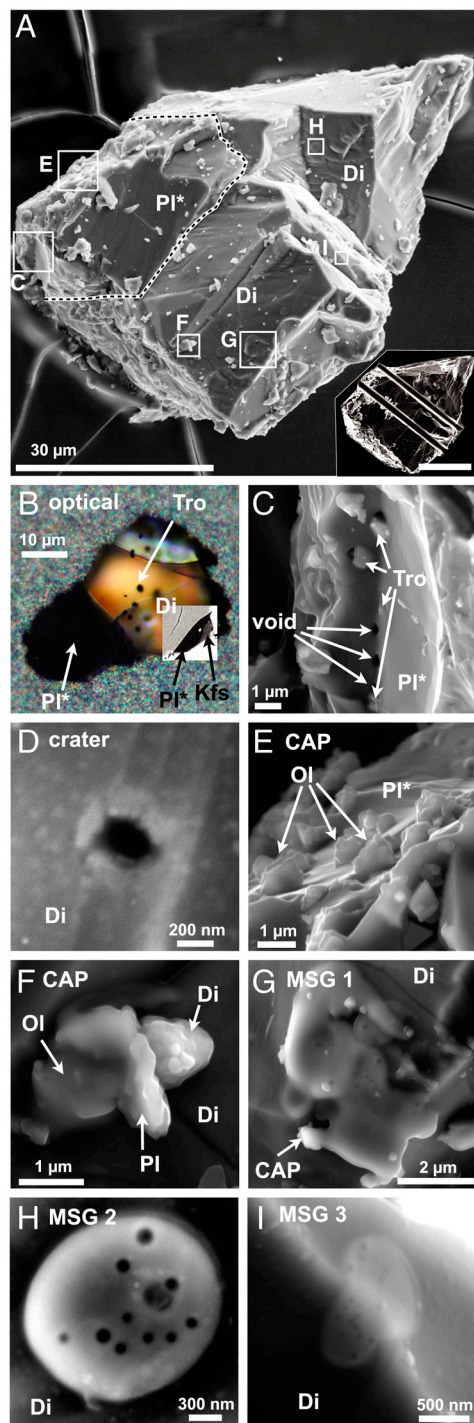


Fig. 3. Surface images of Grain C and its adhered objects, CAPs (common adhered particles) and MSGs (molten splash-shape glasses). (A) Entire Grain C. The grain was cut into three pieces by FIB as shown in the insert in the SE of this image. Di and Pl* indicate diopside and diaplectic plagioclase. (B) Polarized-reflected-light image obtained for the middle slab with thickness of 15 μm . Troilite (Tro) are included in Di. An occurrence of K-feldspar (Kfs) is shown in the inserted BSE image for the SE part of the slab. (C) Microbowls on Pl* substrate partially filled with Tro. Some of these microbowls contain considerable void space. (D) Sub- μm -scale crater on a Di substrate. (E) CAPs on a Pl* substrate. (F) Composite CAP consisting of Ol, plagioclase (Pl), and Di. (G) MSG wrapping around CAPs. (H) Flattened and convex-disk-shaped MSG with degassing vesicles. (I) MSG covering an edge on the surface.

uncertainty of the individual analyses of unknowns is estimated from the spot-to-spot reproducibility (± 1 SD, standard deviation), typically 0.5‰ both for $\delta(^{18}\text{O}/^{16}\text{O})$ and $\delta(^{17}\text{O}/^{16}\text{O})$. The

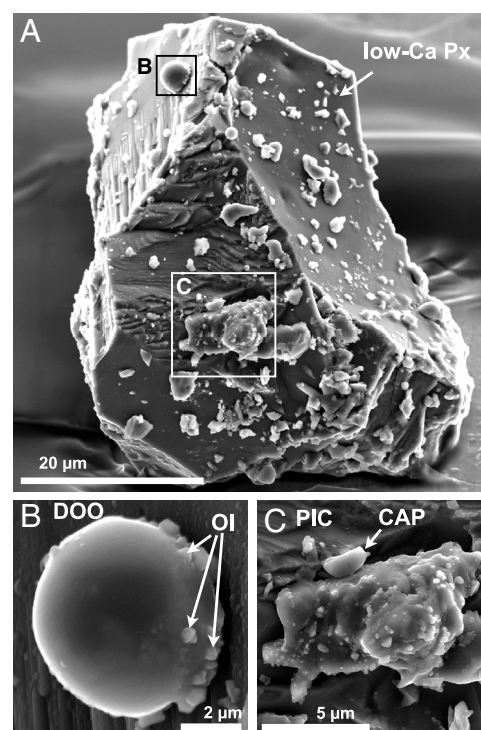


Fig. 4. SEM images of Grain E and adhered objects, DOO (dome-outline objects) and PIC (particularly irregularly-shaped clots). (A) The entire Grain E. (B) DOO and its spherical morphology. Numerous Fe-rich Ol grains are located at the interface between this DOO and its low-Ca pyroxene (low-Ca Px) substrate. (C) PIC consisting of multiple phases, but dominantly sub- μm - to μm -sized merrillite and glass domains and interstitial low-Ca Px and Ol.

in situ analyses demonstrate variation in O isotope compositions within and among phases (Fig. 5A, *SI Appendix*, Table S3), with these compositions scattering around those of whole-rock samples of ordinary-chondrites and forming a cluster elongated with a slope of approximately 0.5. The means of ten analyses are 5.2, 4.1, and 1.4‰ for $\delta(^{18}\text{O}/^{16}\text{O})$, $\delta(^{17}\text{O}/^{16}\text{O})$, and $\Delta(^{17}\text{O}/^{16}\text{O})$ [$\equiv \delta(^{17}\text{O}/^{16}\text{O}) - 0.52 \times \delta(^{18}\text{O}/^{16}\text{O})$], respectively. Although one analysis from Grain C overlaps with the terrestrial fractionation (TF) line, within its 1σ analytical uncertainty, the averages estimated from all grains show $\Delta(^{17}\text{O}/^{16}\text{O}) > 0$. Thus, although the grains have $\delta(^{18}\text{O}/^{16}\text{O})$ values very similar to those of mafic and ultramafic rocks on Earth and the moon, they have $\delta(^{17}\text{O}/^{16}\text{O})$ different from those of the terrestrial lithologies and thus cannot be derived from a reservoir on Earth. Based on these observations, we confirmed that at least four of the grains are extraterrestrial and derived from the asteroid Itokawa.

Materials from Itokawa's Surface. The most abundant mineral phases observed in the five grains are olivine, low-Ca pyroxene, diopside, and plagioclase. This finding is consistent with that of another recent study of the mineralogy of 1,534 grains from Itokawa (6). The individual constituent minerals, in the different grains, have nearly identical major-element compositions (See *SI Appendix*, Table S1). Standard deviations in the Fe/Mg atomic ratios of olivine and pyroxenes are less than 1%. The Fe/Mg ratios of the phases decrease in the order of olivine (highest), low-Ca pyroxene, and diopside (lowest), and Fe/Mn is higher in olivine than in pyroxenes (Fig. 5B). These observations are consistent with the grains having been at an equilibrium condition and, applying two-pyroxene thermometry (16), indicate a temperature of approximately 860°C. Ratios of Fe/Mg and Mn/Fe in olivine and pyroxenes in the Itokawa grains fall within the range for LL-ordinary chondrites (Fig. 5B; ref. 17).

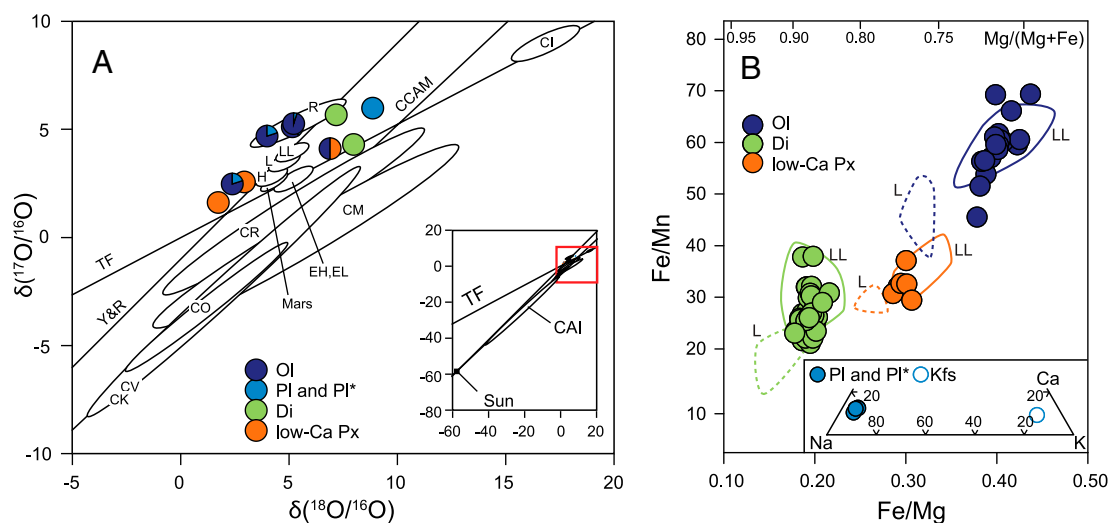


Fig. 5. Oxygen isotope and major element composition. (A) Oxygen three-isotope diagram showing silicate minerals collected by the Hayabusa spacecraft and representative compositions of major primary components of solar system matter. This plot includes bulk-rock data for refractory Ca-Al-rich inclusions (CAIs), carbonaceous, ordinary, enstatite, and R chondrites, and Mars. Ion microprobe data for Ol, Pl, Di, and low-Ca Px are indicated by the colored symbols (blue, light blue, green, and orange, respectively). Overlapping data for multiple phases are shown by the pie charts. The relative dimensions of the probed areas are expressed in the charts accordingly. The data for the minerals from Itokawa grains scatter around the range for whole-rock ordinary chondrites and form an elongated cluster with a slope of approximately 0.5. The means of the analyses for each phase fall into the region for LL-ordinary chondrites defined by Clayton (15). Variation observed in O-isotope compositions is consistent with that observed by Yurimoto, et al. (5) although they interpreted the variation as possibly reflecting analytical ambiguity. (B) A diagram to show relative abundance of Mg-Mn-Fe and Na-K-Ca of silicate minerals from Itokawa grains plotted with those in equilibrated (4–6) ordinary chondrites (L and LL).

The occurrences of diaplectic plagioclase and shock lamellae in the olivine are consistent with shock grade S5 (13). Although the overall variation in $\delta(^{18}\text{O}/^{16}\text{O})$ in the Itokawa grains is 7‰, larger than the 2‰ expected for equilibrium (18), the major element compositional variations and the record of shock-induced deformation preserved in the grains are similar to those noted for equilibrated LL-ordinary chondrites (14). Thus, together, our observations indicate that the uppermost layer of Itokawa's surface is dominantly composed of equilibrated LL-ordinary-chondrite-like material, a conclusion consistent with that of refs. 5, 6 based on study of other grains from Itokawa.

Grain-Surface Observations. Surfaces of the grains from Itokawa retain textures reflecting the environmental conditions that influenced the physical evolution of the asteroid exterior. The grain surfaces are dominated by fractures, and the fracture planes contain sub- μm -sized craters and adhered objects. These observations suggest the importance, at the asteroidal surface, of the destruction of larger-scale lithic materials by external forces such as repeated impact events. In this section, the craters and adhered objects are described in greater detail.

The occurrences of sub- μm -scale craters (100–200 nm in diameter), on the grain surfaces, provide a record of bombardment by nm-scale projectiles (Fig. 2 C–E). Unlike the μm -sized craters with spallation zones developed in lunar samples (19), the rims of the craters on the Itokawa grain consist of chains of seven or eight somewhat irregularly shaped spheres slightly overhanging the pit edges. X-ray mapping (SI Appendix, Fig. S7B) shows that the olivine substrates and the spheres are identical in major element composition, an observation consistent with spheres having been formed from melts of the olivine grains produced by the high-energy impacts. In the Itokawa grains, the bottoms of the pits were not observed. The diameters of the spheres are approximately half the diameters of the pits, thus the minimum depth of the pits can be calculated as being approximately equal to their diameters. Smaller spheres occur around one crater on a diopside substrate without a well developed rim (Fig. 3D), perhaps indicating that the mineralogy of the substrate dictates the morphology of the rim. Assuming that the projectile diameters were an

order of magnitude smaller than the diameters of the pits (20) results in estimated projectile sizes of 10–20 nm. The lunar microcraters show a bimodal size distribution, which is attributed from size of projectiles; craters larger than 5 μm are produced by particles spiraling into the Sun whereas the smaller ones are produced by particles propelled away from the Sun by radiation pressure (21). These smaller particles are referred to as β -meteoroids (traveling at >40 km/s) (22). However, radiation pressure for 10-nm-sized particles is orders of magnitude lower than that for typical β -meteoroids, and another physical process to accelerate nm-sized particles is required to explain the formation of the sub- μm -craters.

The adhered objects are another prominent feature of the grain surfaces (Figs. 3 E–I and 4 B and C). We categorize the adhered objects based on morphology as follows: (i) common adhered particles (CAPs; Fig. 3 E and F) making up 90% of the adhered object population and observed at the surfaces of all grains, (ii) molten splash-shape glasses (MSGs; Fig. 3 G–I) observed on Grains C and D, (iii) dome-outline objects (DOOs; Fig. 4B) that are relatively large (1–3 μm in diameter) and observed on Grain E, and (iv) particularly irregularly-shaped clots (PICs; Fig. 4C), aggregates of several lithic materials (two observed on Grain E only). Following are some preliminary interpretations of these widely varying textures.

The CAPs occur as subrounded or flake-like shapes ranging in size from sub- μm to 5 μm (but mostly approximately 1 μm in size). The CAPs are dominantly composed of individual silicate phases (olivine, low-Ca pyroxene, diopside, plagioclase, K-feldspar, and glass) with subordinate troilite, chromite, Cu-sulfide, and Ca-phosphates. Several of the CAPs are associated with multiple phases such as olivine, diopside, and plagioclase (Fig. 3F). The silicate mineral modes and chemical compositions of the CAPs are consistent with those of host grains, indicating that most CAPs are fragments of larger grains on Itokawa's surface probably formed by impacts. It is possible that some of the CAPs are of exotic origin because Cu-sulfide is not common in L- or LL-chondrites (23). The CAPs are rigidly fixed on surfaces, but the bonding agent remains uncertain. During the electron-probe

work, the interactions of the electron beam with the CAPs did not displace them from the grain surfaces.

The MSGs (Fig. 3 G–I) exhibit irregular shapes (1–5 μm in size) with subcomponents in the shapes of teardrops or rounded disks. MSGs often consist of overlapping layers and appear to wrap around CAPs (Fig. 3G). X-ray mapping (SI Appendix, Fig. S7C) shows that the MSGs and their substrates differ in major element composition. One rounded MSG contains degassing vesicles (Fig. 3H), an observation consistent with the origin of the MSGs as melts. The presence of subrounded features covering the edges of some grains (Fig. 3I) could suggest that melts approached the surface at significant velocity before solidification. Assuming blackbody thermal radiation, residence times for the melts can be roughly estimated to have been on the order of 10^{-3} s; therefore, it is likely that the melting occurred within m-scale distances from their adhesion sites.

The DOOs are characterized as having rounded morphologies. One DOO on Grain E (Fig. 4B) is clearly spheroidal, and this shape and its silica-rich composition ($\text{SiO}_2 \sim 70$ wt.%), suggest that it originated from a relatively viscous melt. Where the DOOs are connected to host objects, rounded sub- μm -sized, Fe-rich olivines are distributed in chain-like fashion. These olivines probably were crystallized from the host melt-spherule during cooling. Unlike for the MSGs, quenching and adhesion appears to have occurred simultaneously for the DOOs. It appears that the transport of silicate melts, likely induced by impacts, was common on the asteroidal surface.

The PIC developed on Grain E (Fig. 4C), 10 μm in its longer dimension, consists of multiple phases but is dominantly composed of sub- μm - to μm -sized merrillite and glass. Analyses of interstitial materials demonstrate that they are olivines and low-Ca pyroxenes (SI Appendix, Fig. S8). The textures and compositions of the PICs indicate that they represent quenched melt pools. Although the presence of the high-pressure polymorph of merrillite could not be confirmed by micro-Raman spectroscopy (SI Appendix, Fig. S9), it is likely that the PICs represent fragments of shock-induced veins, one of the major sites for merrillites observed in ordinary chondrites (24).

In one part of Grain B, three planes were defined based on morphological relationships as F1, F2, and F3, in chronological order assigned by textural observations (Fig. 2A). The oldest plane (F1) on olivine exhibits a scaly fabric (Fig. 2F). We accidentally produced an additional plane by fracturing during laboratory manipulations. This plane, F4, provides another view of the fabric on F1 (Fig. 2G). A sawtooth morphology is observed along F1, and the typical depth and pitch of the sawtooth are 50 and 100 nm, respectively. This sawtooth morphology, not a fracture, suggests on-going modification on F1, and the sharp-edged morphology at the interface suggests that the dominant process was sputtering rather than deposition. The morphology of the scaly fabric implies that surface modification is more effective on physically weaker features such as dislocations related to shock metamorphism. The scaly fabric on F1 suggests that the flux was relatively homogeneous, perhaps pointing to solar wind as the agent for producing this fabric.

Discussion

Asteroid's Surface—Comparison with Spectroscopy. Unprotected by a planetary magnetic field and atmosphere, an asteroid such as Itokawa is continually assailed by micrometeorites and solar wind. In larger-scale studies of asteroid surfaces, based on observations by spectroscopy, the term, space weathering, has become synonymous with darkening or a reduction in band depth in the spectroscopic observations (25). The darkening is thought to reflect the deposition of nano-phase iron on silicate minerals (26) and, accordingly, nano-phase iron particles were found on grains collected from Itokawa (7). Our observations on grain surfaces provide a first demonstration of the sub-micron-scale physical

and chemical properties at asteroid exteriors and indicate that space weathering should be regarded as representing a combination of disaggregation, cratering, melting, adhesion, agglutination, and implantation/sputtering. The deposition of nano-phase iron particles represents one result of this complex set of processes. We note that there are several differences in the factors leading to impact features on asteroids and on the Moon, including micrometeorite impact-velocity, surface mineralogy, and particle-size distributions (27).

Although the number of grains examined here was limited to five, many smaller objects were adhered to the grains' surfaces. As described earlier, most of adhered objects were formed during impacts and are likely representative of the asteroid's surface. We examined 914 adhered objects, randomly chosen from the five grains, for their size and chemical composition. The slope of the cumulative size-distribution, for CAPs as solid fragments with sub- μm to several- μm sizes, is -2.31 regardless of the mineralogy of the fragments (Fig. 6; Dataset S1). This slope is similar to the slope of -2.5 expected for a collisional equilibrium distribution with a mass-independent catastrophic disruption threshold (28). MSGs and DOOs with melt morphology clearly show size distributions different from that for fragments of solids. Differences in these distributions reflect the differing physical properties of the ejecta. The evidence for shock-induced melting suggests impact pressures of 50 to 70 GPa, corresponding to projectile velocities of 5 to 10 km/s (29). Based on semiquantitative analyses, each phase of the 914 objects was determined following an algorithm considering contribution of substrate (SI Appendix, Fig. S11), and modal abundances of the major silicates were estimated to be 32, 23, 16, 3.9, 1.2, and 25 vol.% for olivine, low-Ca pyroxene, plagioclase, diopside, K-feldspar, and glass, respectively (SI Appendix, Table S10). Onboard X-ray fluorescence spectroscopy inferred that the element ratios of Mg/Si and Al/Si of Itokawa's exterior are 0.78 ± 0.09 and 0.07 ± 0.03 , respectively (10), and these ratios are very similar to our ratios of 0.72 and 0.08. Near-infrared spectroscopy (NIRS) provided an olivine/(olivine + pyroxene) modal ratio of 0.7 to 0.8 for the average surface material of Itokawa (9), and this is significantly higher than the es-

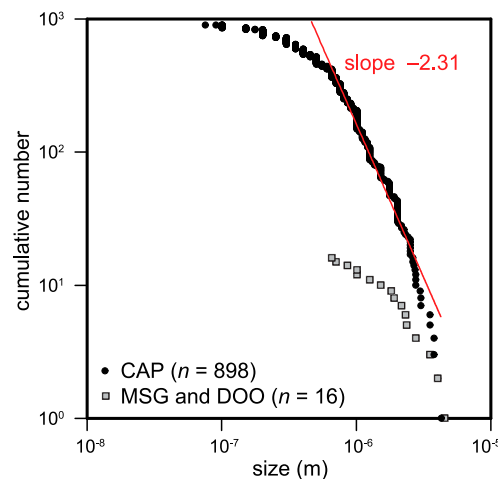


Fig. 6. Cumulative size distribution of solid fragments and quenched melt droplets. Mean of major- and minor-axes of adhered objects randomly chosen was evaluated (Dataset S1). On the log-log plot where grain size is larger than $0.7 \mu\text{m}$, quenched melt droplets (MSGs and DOOs, $n = 16$) yield a slope shallower than that estimated from solid fragments (CAPs, $n = 898$). The distribution could be obtained by the splash of melt droplets associated with the shock-induced melting on Itokawa. In the same range, a best-fit slope for solid fragments yields -2.31 (red line). Particles smaller than approximately $1 \mu\text{m}$ are underrepresented because of their size, therefore, the obtained slope would be somewhat underestimated. The slope suggests catastrophic fragmentation processes by collision cascades might play important role for the evolution of Itokawa's surface.

time of 0.5 resulting from our analysis. A laboratory simulation using ordinary chondrite suggested that impact melting and subsequent crystallization can modify the spectra (30). In our study, a considerable number of glassy particles were observed on the grain surfaces and the absorption effect of these glassy materials is likely underestimated in the previous model based on NIRS results.

Reconstructed Evolution of an Asteroid. Our observations regarding textures, mineralogy, and geochemistry of the Itokawa grains, together with the results of other recent and ongoing studies, allow a tentative reconstruction of the evolution of Itokawa. A K-feldspar included within plagioclase is regarded as an exsolved phase formed during moderately slow-cooling from the peak metamorphic temperature of 860 °C indicated by the equilibrated major element compositions. However, because of the slower diffusion of O relative to that of the major elements, this metamorphism event did not completely erase the O isotope signatures possibly inherited from the building blocks of the asteroid. This inferred thermal history implies the existence of a larger, pre-Itokawa body. An asteroid radius of several tens of km is required to raise temperatures, by decay of short-lived nuclides, sufficiently to equilibrate silicate major element compositions at temperatures near 900 °C (31). Such temperatures cannot have been attained on the current Itokawa, with its radius of only 300 m. Shock-induced properties such as shock lamellae and diaplectic plagioclase, and the occurrences of PICs, could be indicative of the collisional break-up of a larger asteroid body, the fragments from which were accreted to form the current Itokawa.

It is difficult to ascertain the exact characteristics of the projectiles whose impacts shaped Itokawa's surface; however, the projectiles must have impacted at a significant range of "hypervelocities" to create the nano-size craters and produce adhered objects, including melts, in the inferred sustained fashion. Because of the low escape velocity on Itokawa and on other similar bodies, it is likely that such asteroids are major sources of interplanetary dust particles.

We suggest that the chemistry and textures of Itokawa's surface reflect long-term bombardment of equilibrated chondritic material, at scales of 10^{-9} to 10^4 meters, and that impact processes in general play a central role in the evolution of planetary bodies. Further surface observations on grains returned by Hayabusa will add statistical significance to the insights regarding solid-to-solid interactions fundamental to our understanding of asteroid accretion and, more broadly, the formation and evolution of interplanetary objects. Needless to say, sampling on other asteroids, and acquisition of age constraints for these bodies, should be the next major conquest.

Materials and Methods

All analyses were undertaken at the Pheasant Memorial Laboratory with nm-scale sample handling capability in part demonstrated by Nakamura, et al. (32). During our study of the Hayabusa grains, we (i) determined optical properties, (ii) described surface textures and identified constituent phases using a field-emission-type scanning electron microscope (SEM), (iii) produced slabbed samples of the grains using a FIB, (iv) investigated major element compositions by electron-microprobe techniques, and (v) performed in situ analyses, including measurements of O-isotope composition, by SIMS. In this paper, we in particular focused on the grain surface morphology and mineralogy reflecting the physical environment at the asteroidal surface. Greater detail regarding this work is provided in the [SI Appendix](#), file linked to the online version of this paper. This file provides Supplemental Methods, Discussion, Tables, Figures, and References related to this initial analysis, including trace-element compositions obtained by SIMS.

ACKNOWLEDGMENTS. The comprehensive analysis we undertook was only possible working as a team. We thank Ikuo Kushiro and the pheasant that in 1992 unknowingly helped launch us on our intellectual quest. We are greatly indebted to T.A. Chekol and S. Tokeshi for their assistance maintaining the laboratory and we thank T. Yamamoto, T. Kadono, S. Ohno, and S. Sasaki for helpful discussions. We are grateful for G. Bebout's efforts editing for clarity and we thank T. Yokoyama, T. Kuritani, and H. Takei for their assistance with the development of analytical methods during the initial stages of our study. Finally, we thank the two anonymous reviewers for their constructive comments.

- Fujiwara A, et al. (2006) The rubble-pile asteroid Itokawa as observed by Hayabusa. *Science* 312:1330–1334.
- Saito J, et al. (2006) Detailed images of asteroid 25143 Itokawa from Hayabusa. *Science* 312:1341–1344.
- Demura H, et al. (2006) Pole and global shape of 25143 Itokawa. *Science* 312:1347–1349.
- Yano H, et al. (2006) Touchdown of the Hayabusa spacecraft at the Muses Sea on Itokawa. *Science* 312:1350–1353.
- Yurimoto H, et al. (2011) Oxygen isotopic compositions of asteroidal materials returned from Itokawa by the Hayabusa mission. *Science* 333:1116–1119.
- Nakamura T, et al. (2011) Itokawa dust particles: a direct link between S-type asteroids and ordinary chondrites. *Science* 333:1113–1116.
- Noguchi T, et al. (2011) Incipient space weathering observed on the surface of Itokawa dust particles. *Science* 333:1121–1125.
- Tsuchiyama A, et al. (2011) Three-dimensional structure of Hayabusa samples: origin and evolution of Itokawa regolith. *Science* 333:1125–1128.
- Abe M, et al. (2006) Near-infrared spectral results of asteroid Itokawa from the Hayabusa spacecraft. *Science* 312:1334–1338.
- Okada T, et al. (2006) X-ray fluorescence spectrometry of asteroid Itokawa by Hayabusa. *Science* 312:1338–1341.
- Muller WF, Hornemann U (1969) Shock-induced planar deformation structures in experimentally shock-loaded olivines and in olivines from chondritic meteorites. *Earth Planet Sci Lett* 7:251–264.
- Weisberg MK (1987) Barred olivine chondrules in ordinary chondrites. *J Geophys Res* 92(B4):663–678.
- Stöffler D, Keil K, Scott ERD (1991) Shock metamorphism of ordinary chondrites. *Geochim Cosmochim Acta* 55:3845–3867.
- Kovach HA, Jones RH (2010) Feldspar in type 4-6 ordinary chondrites: metamorphic processing on the H and LL chondrite parent bodies. *Meteorit Planet Sci* 45:246–264.
- Clayton RN (2003) Oxygen Isotopes in Meteorites. *Meteorites, Comets and Planets: Treatise on Geochemistry*, ed AM Davis pp:129–142.
- Brey G, Kohler T (1990) Geothermobarometry in four-phase lherzolites II. New thermo-barometers, and practical assessment of existing thermobarometers. *J Petrol* 31:1353–1378.
- Gastineau-Lyons HK, McSween HY, Jr, Gaffey MJ (2002) A critical evaluation of oxidation versus reduction during metamorphism of L and LL group chondrites, and implications for asteroid spectroscopy. *Meteorit Planet Sci* 37:75–89.
- Clayton RN, Onuma N, Mayeda TK (1976) A classification of meteorites based on oxygen isotopes. *Earth Planet Sci Lett* 30:10–18.
- Horz F, et al. (1975) Lunar microcraters: implications for the micrometeoroid complex. *Planet Space Sci* 23:151–152.
- Holsapple KA (1993) The scaling of impact processes in planetary sciences. *Annu Rev Earth Pl Sci* 21:333–373.
- Morrison DA, Zinner E (1977) 12054 and 76215—new measurements of interplanetary dust and solar flare fluxes. *Proc Lunar Sc Conf, 8th*, 1 pp:841–863.
- Carpenter JD, et al. (2007) Nanometer hypervelocity dust impacts in low Earth orbit. *J Geophys Res Planet* 112(E08008), doi:10.1029/2007JE002923.
- Rubin AE (1997) Mineralogy of meteorite groups. *Meteorit Planet Sci* 32:231–247.
- Llorca J, Trigo-Rodríguez JM (2006) Raman spectroscopy of merrillite in Villalbeto de la Peña L6 ordinary chondrite. *Lunar Planet Sci XXXVII abstr*:1055.
- Hapke B (1993) *Theory of Reflectance and Emittance Spectroscopy* (Cambridge University Press, New York) p 455.
- Sasaki S, Nakamura K, Hamabe Y, Kurahashi E, Hiroi T (2001) Production of iron nanoparticles by laser irradiation in a simulation of lunar-like space weathering. *Nature* 410:555–557.
- Gaffey MJ (2010) Space weathering and the interpretation of asteroid reflectance spectra. *Icarus* 209:564–574.
- Tanaka H, Inaba S, Nakazawa K (1996) Steady-state size distribution for the self-similar collision cascade. *Icarus* 123:450–455.
- Melosh HJ (1989) *Impact Cratering: A Geologic Process* (Oxford University Press, New York) p 253.
- Moroz LV, Pieters CM, Korotaeva NN (1996) Optical effects of regolith processes on S-asteroids as simulated by laser shots on ordinary chondrite and other magic materials. *Icarus* 122:366–382.
- Kunihiro T, Rubin AE, McKeegan KD, Wasson JT (2004) Initial $^{26}\text{Al}/^{27}\text{Al}$ in carbonaceous-chondrite chondrules: Too little ^{26}Al to melt asteroid. *Geochim Cosmochim Acta* 68:2947–2957.
- Nakamura E, et al. (2003) Comprehensive geochemical analyses of small amounts (<100 mg) of extraterrestrial samples for the analytical competition related to the sample return mission MUSES-C. *ISAS Report SP The First Open Competition for the MUSES-C Asteroidal Sample Preliminary Examination Team* 16:49–101.